-Supporting information-

Hydrogen-Bonding Guar Gum Stabilizes Solid-State Si Anodes

Hongbo Shu[a], Qinghuang Lian[b], Chenyang Gu[b], Le Yang[b], Chuangchuang Duan[b], Weihua Yang[b], Jing Li[a], Chenji Hu[c]*, and Hongwei Chen[b]**

[a] *School of Materials Science and Engineering, Hunan University of Technology, Zhuzhou 412007, PR China*

**Jing Li, E-mail: lijingsinano@163.com*

[b] *College of Materials Science and Engineering, Huaqiao University, Xiamen, Fujian Province, 361021, China.*

**Hongwei Chen, E-mail: hwchen@hqu.edu.cn*

[c] *School of Chemistry and Chemical Engineering, in-situ Center for Physical Sciences, Shanghai Jiao Tong University, Shanghai 200240, P. R. China.*

**Chenji Hu, cjhu2014@sjtu.edu.cn*

Contents

Electrode preparation. The microsilicon and guar gum (GG) aqueous solution (1 wt%) was mixed and ground for 1 h to obtain a uniform slurry, which was then coated onto a copper foil current collector through a 70 μm doctor blade. Place it in a vacuum oven at 80°C overnight, and finally cut the Si@GG electrode into circular electrodes with a diameter of 10 mm. Similar method is used to fabricate the Si@PVDF electrode, where the guar gum aqueous solution is replaced by the N-methylpyrrolidone solution of PVDF. The binder-free Si electrode was prepared by replacing the GG aqueous solution by deionized water. Then, the lithium cobalt oxide ($LiCoO_2$) cathode material for solid-state batteries was prepared. 140 mg of $LiCoO_2$, 56 mg of Li_6PS_5Cl and 4 mg of VGCF were weighed accurately and transferred into a mortar, followed by manual grinding for 45 min until the mixture was homogeneous. Finally, the ground composite powder was collected and stored in a sealed bottle.

Solid-state battery assembly. First, 80 mg of Li_6PS_5Cl is pressed between two steel rods at a pressure of 125 MPa for 1 min to form a 10 mm diameter solid electrolyte. Then, a Si@GG working electrode is added to the cathode tab and pressed at 375 MPa for 3 min. After that, a lithium-indium (Li-In) alloy (mass ratio Li:In=1:30) is added to the anode tab. Finally, the completed battery is packaged under a working pressure of 50 MPa. For the all-solid-state battery assembly, first, 80 mg of Li_6PS_5Cl is pressed between two steel rods at a pressure of 125 MPa for 1 min to form a 10 mm diameter solid electrolyte. Then, 11.5 mg of cathode active material (mass ratio of $LiCoO_2$:Li_6PS_5Cl:VGCF=70:28:2) is added to the cathode side and pressed at 375 MPa for 3 min. After that, the Si@GG electrode is added to the anode side and pressed at 375 MPa for 3 min, with an N/P ratio of 1.3. Finally, the completed battery is packaged under a working pressure of 50 MPa. All the cell assembly processes were performed inside an argon-filled glovebox.

Material characterization. Morphology characterization was conducted on a scanning electron microscope (SEM, SU8010, HITACHI) operated at an accelerating voltage of 5 kV. The chemical valence states of the samples were obtained by X-ray photoelectron spectroscopy (XPS, Thermo Fisher ESCALAB 250X), and all binding energy values were calibrated to the peak c1s 284.8 eV. The crystal structure of the samples were obtained by X-ray diffractometer (XRD, D8 Advance, Bruker) using Cu Kα radiation (=0.15406 nm) over a range of 10°-90° with the instrument operating at 40 kV and 40 mA. The functional groups were collected by Fourier transform infrared spectrometer (FTIR, Nicolet iS 50). The nanoscratch tests of Si@PVDF and Si@GG electrodes were carried out using the MST Agilent G200 nanoscratch tester. The mechanical properties of GG were characterized by a universal tensile testing machine (UTM) in accordance with standard testing protocols.

Electrochemical measurements. Electrochemical performance, including rate capability and cycling stability, was evaluated using a NEWARE battery testing system (CT-4008 Tn-5V10 Ma-164, NEWARE Technology Co., Ltd., Shenzhen, China), within a voltage window of -0.6–1.0 V vs. Li^+/Li. The nominal specific capacity was defined as 1 C=3590 mAh g^{-1}. Cyclic voltammetry (CV) measurements were conducted on an electrochemical workstation (CHI760E, Shanghai, China) at a scan rate of 0.2 mV s^{-1}. Electrochemical impedance spectroscopy (EIS) was also performed on the same electrochemical workstation with the frequency range spanning from 1 MHz to 0.01 Hz. The electronic conductivity of the materials was primarily measured via the four-probe method. All electrochemical performance tests in this study were consistently conducted under controlled ambient conditions at 25°C.

Theoretical calculations. The lattice parameters of bulk Si were optimized using the CASTEP module. The calculations employed the Perdew–Burke–Ernzerhof exchange–correlation functional under the generalized gradient approximation along with OTFG ultrasoft pseudopotentials. Based on the optimized bulk structure, a Si (100) surface model was constructed by cleaving the crystal along the (100) direction. A vacuum layer of 15 Å was introduced along the surface normal to avoid periodic interactions, resulting in a 2×3 surface supercell. Subsequently, geometric optimization of the constructed surface model was performed under the same computational settings.Furthermore, GG and PVDF were individually adsorbed onto the Si (100) surface, and their adsorption configurations were geometrically optimized using the same functional and pseudopotentials. The adsorption energy was calculated in a manner consistent with the binding energy, defined as follows: $E_{ads}=E_{AB}-E_A-E_B$ .where E_{AB} is the total energy of the adsorption system, E_A is the energy of the clean Si (100) surface, and E_B is the energy of the isolated molecule.

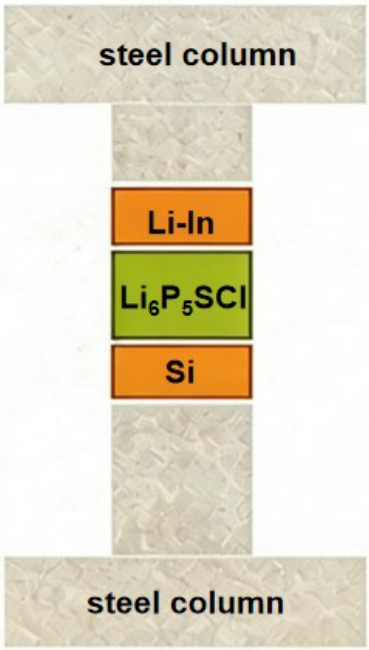

Fig. S1. The construction of the solid-state battery.

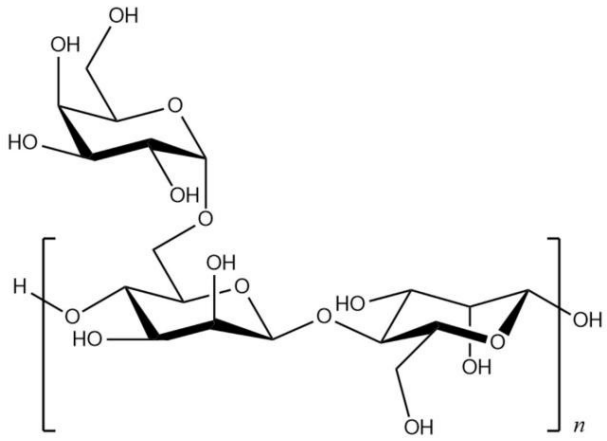

Fig. S2. The structure of guar gum.

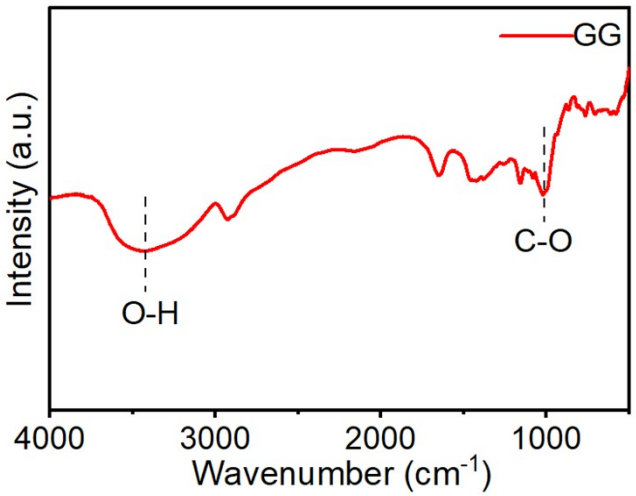

Fig. S3. Infrared spectrum of guar gum.

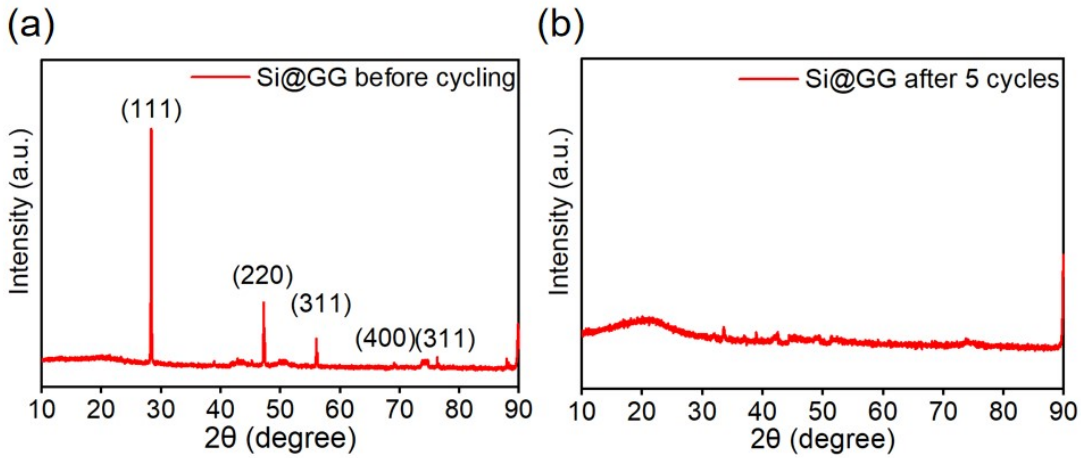

Fig. S4. XRD patterns of Si@GG before (a) and after cycling (b).

Compared with Si@GG before cycling, the XRD pattern of Si@GG after cycling shows no crystalline silicon peaks after 5 cycles, indicating that the crystalline silicon has completely transformed into amorphous silicon after 5 cycles.

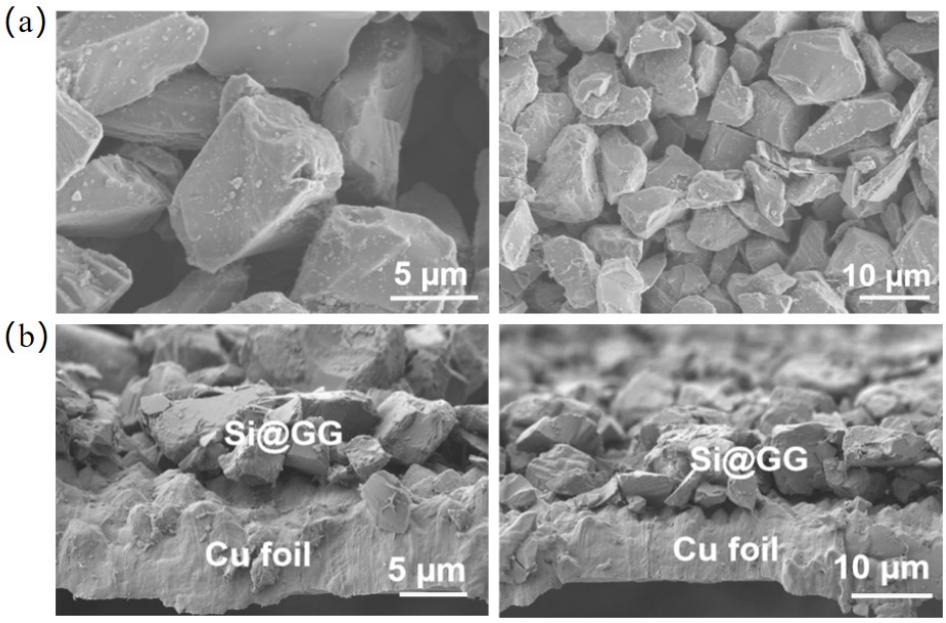

Fig. S5. (a) SEM images of the Si@GG anode before cycling. (b) Cross-sectional SEM images of the Si@GG anode before cycling.

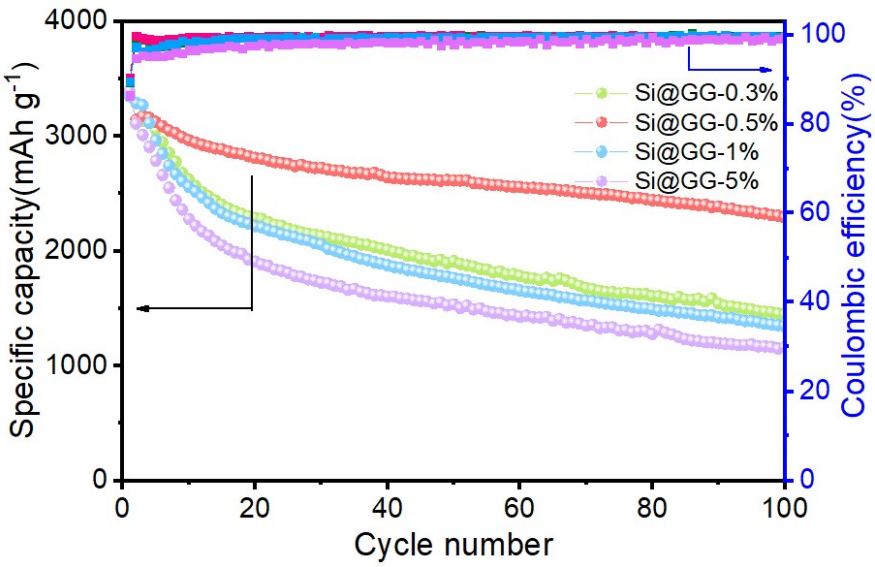

Fig. S6. Cycling performance of the Si anode with different GG contents.

Si@GG-0.5wt% exhibits the best overall performance: it maintains a relatively high initial capacity while showing significantly better cycling stability than other components, indicating that at this content, GG can effectively buffer the volume expansion of silicon during cycling and maintain electrode structure stability. Therefore, an addition of 0.5% GG represents the optimal amount in this system.

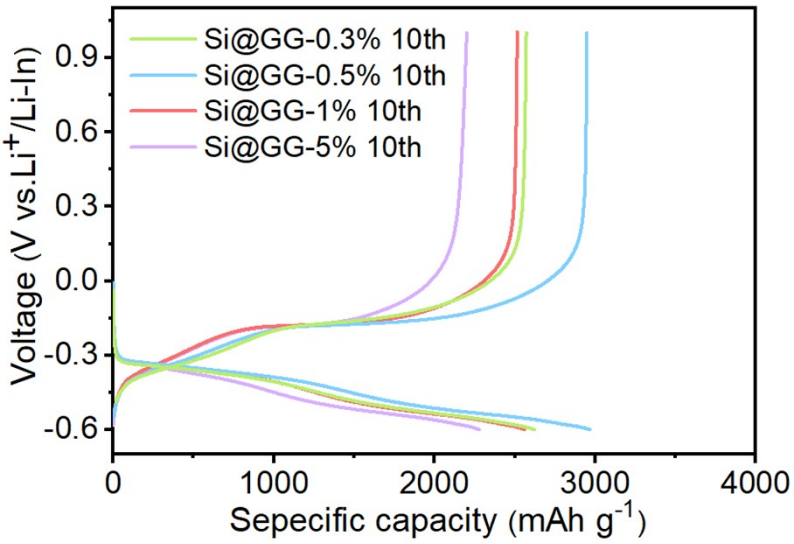

Fig. S7. The charge-discharge curves of the Si@GG-0.5wt% anode.

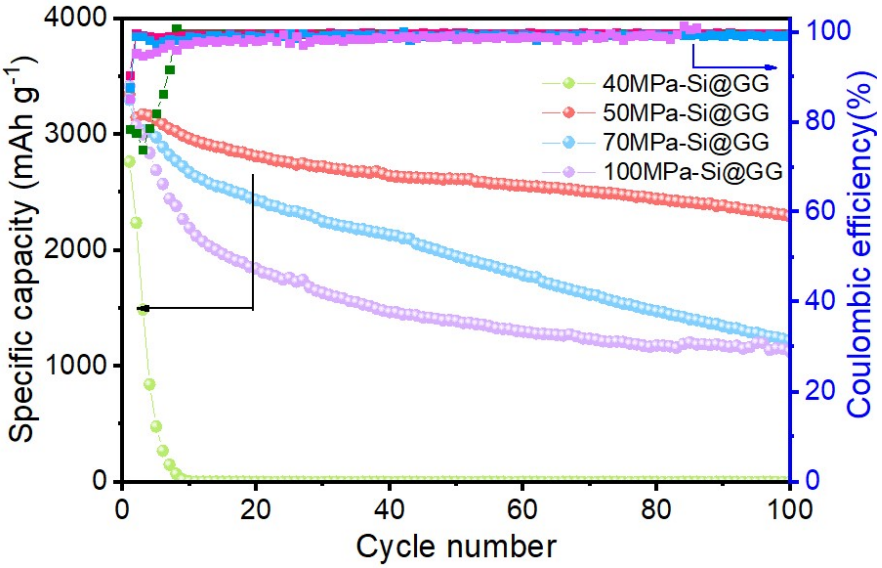

Fig. S8. Cycling performance of the Si@GG anodes under different pressures.

The electrode demonstrates optimal cycling stability under an external pressure of 50 MPa. Despite its moderate initial capacity (3347.80 mAh/g), it undergoes the slowest capacity decay during long-term cycling and achieves the highest capacity retention. At 100 MPa, the electrode delivers a higher initial capacity (3417.83 mAh/g) but suffers from accelerated capacity fading. This suggests that excessive pressure may induce internal stress accumulation and interfacial damage within the electrode, which is detrimental to long-term cycling performance. The electrochemical performance at 70 MPa is intermediate between the two aforementioned pressures, with both initial capacity and cycling stability showing moderate characteristics.When subjected to a working pressure of 40 MPa, the battery showed no residual capacity after 10 charge-discharge cycles, indicating severe performance degradation.

Under an operating pressure of 50 MPa, the Si@GG composite exhibits an initial discharge capacity retention of 90.40%, which is significantly higher than those of the batteries tested under operating pressures of 40 MPa (78.42%), 70 MPa (87.68%), and 100 MPa (85.25%), respectively.

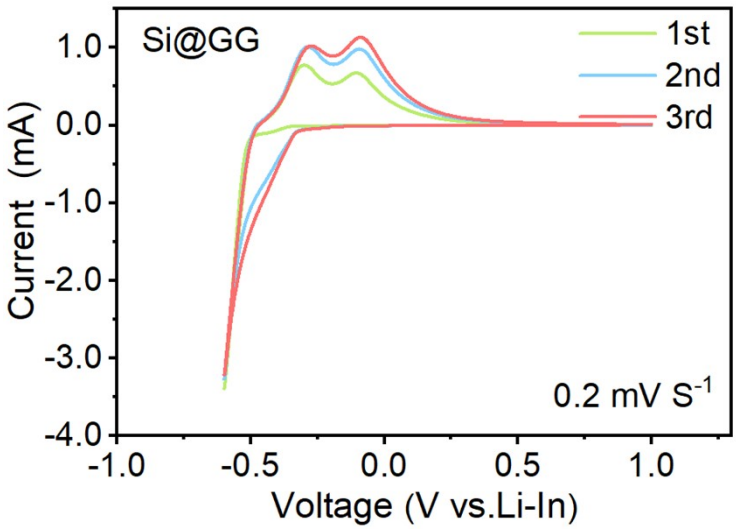

Fig. S9. CV Curves of the Si@GG anode.

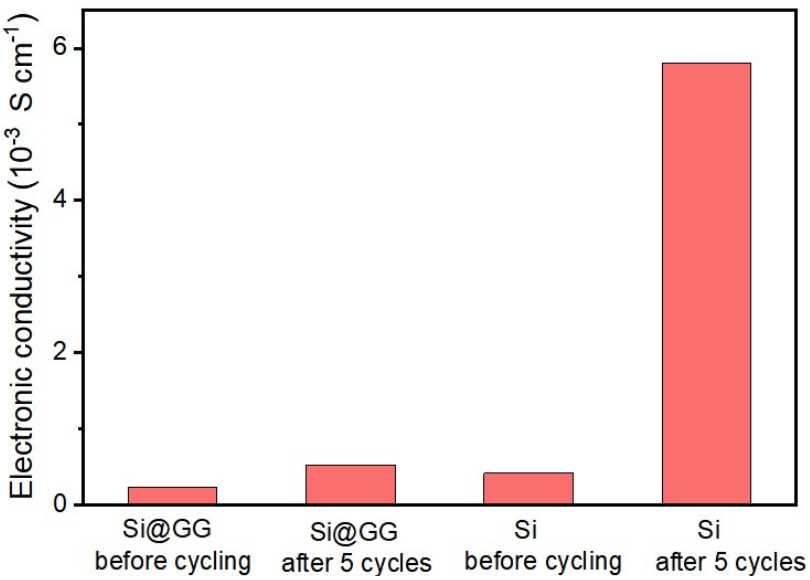

Fig. S10. Electrical conductivity of Si and Si@GG electrodes.

The electronic conductivity of the Si@GG composite before cycling is significantly lower than that of pure silicon. However, after five extended cycles, the conductivity of both electrodes increases markedly, suggesting the formation of LixSi phases during cycling. Notably, the electronic conductivity of the cycled pure Si anode remains nearly an order of magnitude higher than that of the cycled Si@GG. Given that LixSi exhibits higher electronic conductivity than pure Si, these results indicate that lithium extraction is less complete in the pure Si anode, leaving a higher residual content of conductive LixSi within the material.

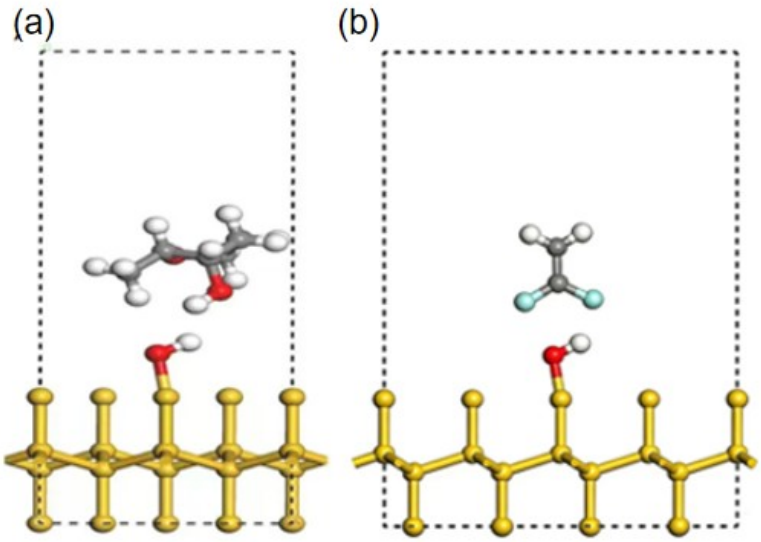

Fig. S11. DFT-based adsorption force model for Si@GG (a) and Si@PVDF (b).

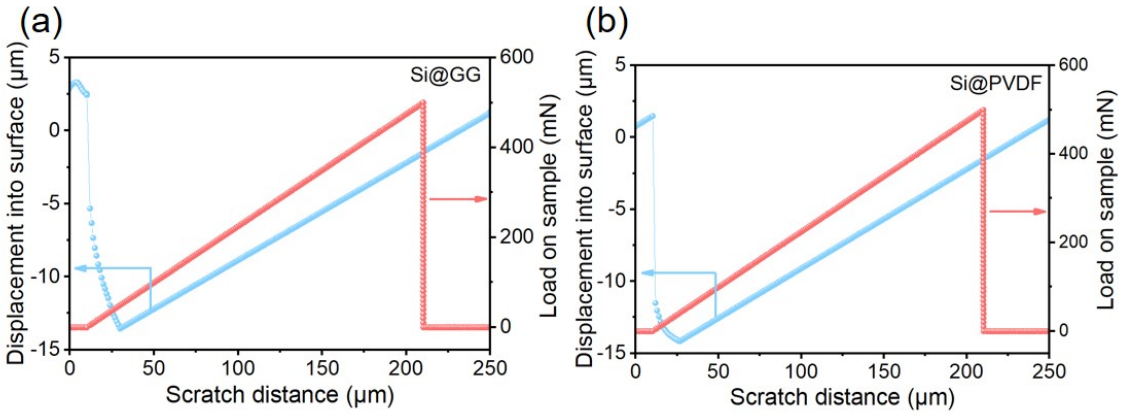

Fig. S12. Nanoscratch tests of Si@GG (a) and Si@PVDF electrode (b).

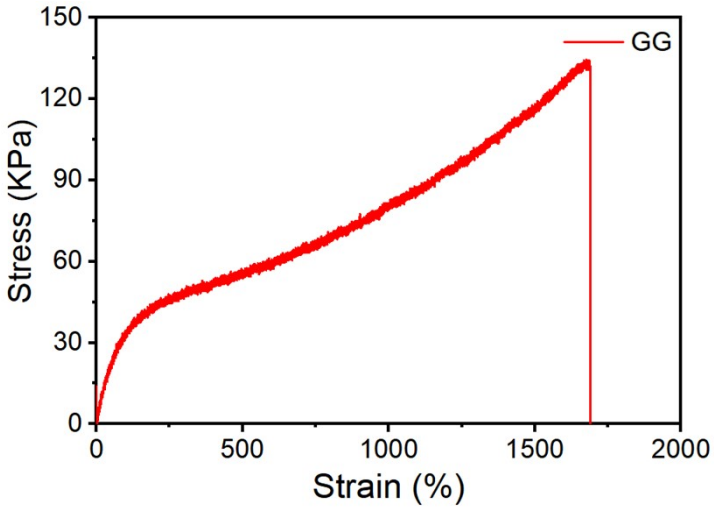

Fig. S13. Stress-strain curve of guar gum film.

The GG film (formed by 10 wt% aqueous GG solution) exhibits high mechanical toughness and exceptional deformability. Such large deformation capability suggests that GG is well suited to accommodate the substantial volume expansion of Si anodes during lithiation, thereby helping to preserve electrode integrity in solid-state batteries.

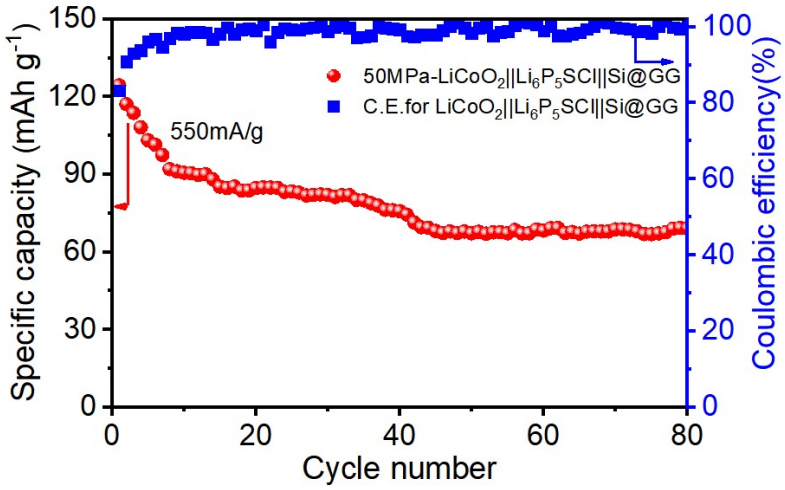

Fig. S14. Cycling performance of the Si@GG‖$LiCoO_2$ all-solid-state cell measured between 3.0-4.2 V under 50 MPa.

Table S1. Comparison of first charge-discharge specific capacity, initial Coulombic efficiency, and capacity retention over 100 cycles for different Si anodes.

Anode	Initial discharge capacity (mAh/g)	Initial coulombic efficiency (%)	100-cycle capacity retention (%)
Si	2965.85	78.36	12.63
Si@PVDF	3026.68	81.39	63.81
Si@GG	3347.80	90.40	68.45

Table S2. Impedances of Si, Si@PVDF, and Si@GG at different cycle numbers.

Anode	Si		Si@PVDF		Si@GG	
R	Rs/Ω	Rct/Ω	Rs/Ω	Rct/Ω	Rs/Ω	Rct/Ω
Before cycling	14.61	3.12	15.10	2.16	14.12	2.07
After 1 cycle	18.96	7.02	22.83	5.92	15.99	5.06
After 10 cycles	26.07	14.20	23.59	8.42	16.08	3.93
After 50 cycles	26.80	30.17	23.13	34.46	18.62	12.57

Table S3. Electronic conductivity of Si and Si@GG before and after cycling.

Anode	Before cycling (S cm^{-1})	After 5 cycles (S cm^{-1})
Si	$4.117*10^{-4}$	$5.81*10^{-3}$
Si@GG	$2.241*10^{-4}$	$5.21*10^{-4}$

Table S4. Comparison of binders for silicon-based anodes in Lithium-ion batteries.

Binder types	Initial discharge capacity (mAh/g)	Initial coulombic efficiency	100-cycle capacity retention	Current Density (mA g^{-1})	Battery type	Ref.
PAA-PVA	3616	83.90%	63.14%	400	liquid battery	[1]
PAA-PEGPBI	1292	87.30%	58.13%	130	liquid battery	[2]
NaPAA-g-CMC	2290	84%	79.30%	840	liquid battery	[3]
PAA-VTEO	470	89.40%	99.19%	47	liquid battery	[4]
CMC-CA	1870	74%	87.70%	1000	liquid battery	[5]
PAAS-β-CDp-PAA	3534	89.79%	71.10%	200	liquid battery	[6]
PEDOT:PSS	2600	78%	75%	1000	liquid battery	[7]
PEDOT-PSS-PMA	2380	70%	80% (50cycles)	700	solid-state battery	[8]
PVDF	3500	83%	29.6%	350	solid-state battery	[9]
GG	3348	90.40%	68.5%	350	solid-state battery	This work

References

[1] J. Song et al., *Adv. Funct. Mater.*, 2014, **24**, 5904–5910.

[2] T. H. Kim et al., *ACS Appl. Mater. Interfaces*, 2015, **7**, 23545–23553.

[3] L. Wei et al., *Sci. Rep.*, 2016, **6**, 19583.

[4] S. Liu et al., *J. Polym. Sci.*, 2021, **60**, 1835–1844.

[5] Y. Liu et al., *Adv. Mater*., 2017, **29**, 1703028.

[6] F. Zheng et al., *J. Alloys Compd*., 2023, **932**, 167666.

[7] T. M. Higgins et al., *ACS Nano,* 2016, **10**, 3702–3713.

[8] S. Jun et al., *Nat. Commun*., 2025, **16**, 1234.

[9] H. Huo *et al.*, *Nat. Mater.*, 2024, **23**, 543.